Advances in Computational Design, *Vol. 9, No. 3 (2024) 229-252*
https://doi.org/10.12989/acd.2024.9.3.229

Simulating flow-induced fiber motion with finite element based explicit coupling method

Diwei Zhang*, Xiaobo Peng[a] and Dongdong Zhang[b]

Department of Mechanical Engineering, Roy G. Perry College of Engineering, Prairie View A&M University, 700 University Drive, Prairie View, Texas 77446, U.S.A.

(Received June 6, 2019, Revised May 11, 2022, Accepted September 11, 2024)

Abstract. This paper presents a finite element based explicit coupling method. The derived method is proposed to solve a certain type of fluid-structure interaction problem, which is the motion of a single or flexible fiber with the motion induced by the low-Reynolds-number fluid. The particle motion is treated as a non-linear geometric dynamic problem. The Total-lagrangian finite element method is applied to describe and discretize the particle domain. The Bathe method is used to integrate the time domain. The Stokes equation is used as the governing equation of the fluid domain. The inertia term of the Stokes equation is ignored, and Reynolds number flow is assumed as zero. Since the time term is also canceled, we solve it as a quasi-static problem. Mixed finite element is to solve the fluid equation. An explicit strategy is implemented to couple the particle and the zero-Reynolds number flow. Simulations with the proposed method are presented, including the motion of single and double rigid particle immersed in the double Couette flow and the Poiseuille flow. Simulation of single flexible fiber immersed in a Poiseuille flow is also presented. Effect of particle's density, aspect ratio, and geometry are discussed.

Keywords: finite element method; fluid-structure interaction; non-linear geometric solid; Stokes equation

1. Introduction

The low Reynolds number flow-induced particle motion phenomenon occurs in different areas. In the injection molding processing of manufacturing the short-fiber reinforced composite material (Callister 2009), flow-induced fiber motion takes place in the injection processing. Fibers rotate and translate in the matrix until injection processing completes, and a certain fibers distribution and orientation have been formed (Papathanasiou and Guell 1997). Since fibers distribution and orientation determine the properties of composite material, such as strength, stiffness, thermal conductivity, it is necessary to predict or control the fibers' motion in the injection processing to ensure the final composite material meets requirements (Courtney 2005). Similarly, in the papermaking industry, wood pulp motion in the making process can be classified as flow-induced flexible fiber motion problems. Quality of paper products depends on the distribution and the

*Corresponding author, Ph.D. Student, E-mail: dzhang2@student.pvamu.edu
[a] Professor, E-mail: xipeng@pvamu.edu
[b] Ph.D., E-mail: peterzdd_2002@hotmail.com

http://www.techno-press.org/?journal=acd&subpage=7 ISSN: 2383-8477 (Print), 2466-0523 (Online)

orientation of the fibers in the pulp (Stockie and Green 1998). In medical science, blood cell motion in the vessel is a flow-induced particle motion problem (Tan *et al*. 2016). Investigation of the cell's motion can provide us a better understanding of some diseases. In biology, the study of the microorganism locomotion involves the modeling of flagella which is a fluid-structure interaction problem in low Reynolds number flow (De Corato *et al*. 2015).

The flow-induced particle motion problem has been investigated over one hundred years. Many analytical and experimental works have been conducted, which revealed the basic characteristics of the problem. Later, computational methods have played an important role in solving more complex conditions of flow-induced particle motion problems. Some methods can simulate flow-induced rigid particle motion problems successfully in certain conditions. Moving mesh, interface between the particle and the fluid, and the stability of simulation is still the bottleneck of the research on those problems. The simulation of flow-induced flexible fiber motion is a more challenging problem. Bead-chain model or beam-chain model were applied widely on the modeling of the flexible fiber. Only slender-shape particles can be simulated with those models. Using those models also involves unnecessary complex work compared to using a simpler and more popular structural finite element model, such as a solid element or beam element. In general, most of existing computational methods have certain limitations, and there is no standard way to simulate flow-induced particle motion problems.

The goal of this research is to derive a computational method to simulate the low Reynolds number flow-induced particle motion problem. The derived method is able to address the different shape of particles. It is also able to simulate rigid particles and flexible particles. The quasi-static Stokes equation was applied as the governing equation of the fluid domain which was solved by the finite element method. The particle was treated as a non-linear geometric problem. The Total-Lagrangian (TL) finite element was used to discretize the particle. The Bathe method was applied to integrate the particle's dynamic motion over the time domain. A serial partitioned coupling method was derived to couple the fluid and solid domains. Other contributions of this paper include that the influence of density of particle on the flow-induced particle motion was investigated with the derived method. The influence of the geometry and the shape of the particle, the phenomenon of multi-particle motion in the Couette flow, and flexible fiber motion in the Poiseuille flow were also studied.

The paper is organized as follows. In the related work section, important theoretical, experimental, and computational work on flow-induced particle motion problems are introduced. In the methodology section, solution of fluid, solution of particle, coupling strategy, and solution of multi-particle motion are discussed. Finally, in the section of results, the verification of the derived method is presented first. By using the derived method, result of simulations of flow-induced different density of particles, different shape of particles, and different aspect ratio of particles are presented. Flow-induced multi-particle motion and flexible fiber motion were also demonstrated with the derived method.

2. Problem

Jeffery (1922) generated a formula mathematically to describe an orbit of a rigid ellipsoid particle immersed in the shear flow. Zero inertia of both fluid and particle was an assumption. Fluid domain is assumed infinite large to avoid boundary effect on the motion of the particle. Jeffery's theory is the foundation of theoretical works concerning this problem. Two-dimensional Jeffery theory is described in Eq. (1.1).

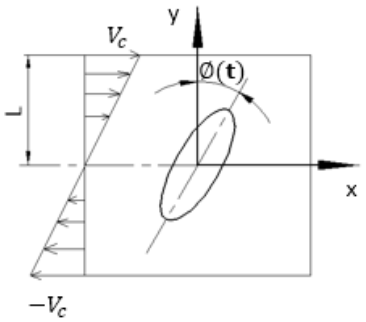

Fig. 2.1 An illustration of an ellipsoid fiber immersed in the double Couette flow

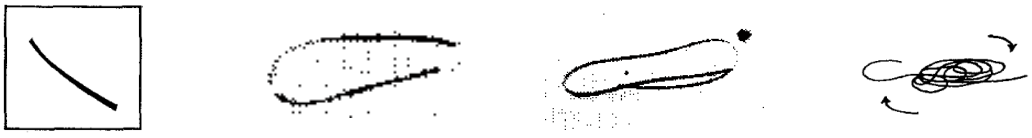

(a) (b) (c) (d)

Fig. 2.2 Deformation of different length of threadlike particles. (a) Springy rotation; (b) Snake rota tion; (c) Helix rotation; (d) Coil formation

$$\emptyset(t) = tan^{-1}(r_e tan\frac{\dot{\gamma}t}{r_e + 1/r_e}) \tag{1.1}$$

Fiber's rotation angle $\emptyset$ is a time-dependent variable. Ellipsoid aspect ratio is represented by r_e. Time t is the variable of the equation. Flow shear rate $\dot{\gamma}$ can be calculated by equation $\dot{\gamma} = V_c/L$, where V_c is the characteristic velocity and L is the height of simple shear flow. Fig. 2.1 illustrates an ellipsoid fiber immersed in a double Couette flow and the mentioned notations applied in Jeffery's theory.

Jeffery's theory reveals that fiber's angular velocity increases with the increase of flow shear rate. An ellipsoid fiber's angular velocity reaches the maximum while the fiber's long axis orientation is perpendicular to the flow shear direction. An ellipsoid fiber's angular velocity reduces to the minimum while the fiber's long axis orientation is parallel to flow shear direction.

Most of the theoretical works regarding flow-induced rigid particle motion are the extension of Jeffery's theory. In Ho and Leal's (1974) study, non-Newtonain effect and weak inertial of fluid were involved. It was concluded that axisymmetric but non-spheroid particles generally show the same behavior in the shear flow as a spheroid particle. Stover and Cohen's (1990) experimental results agreed with Jeffery's theory and Leal's theory quantitatively.

Particle's lateral migration was another essential topic in the field of flow-induced particle motion. Segré and Silberberg (1961) found that a rigid sphere particle always migrates to a certain region of the channel in the Poiseuille flow, wherever particles were released. Segré-Silberberg effect was named after them. Bretherton (1962) proved that no lateral migration can be observed in the very low Reynolds number flow theoretically. The inertia force and the non-Newtonian effect can be neglected because of the extremely low Reynolds number. Therefore, there is no lateral migration taking place no matter what the shape of the particle is.

Folgar and Tucker III (1984) derived an orientation distribution function of the concentrated suspensions. Even their theory predicted more rapid alignment than actual is, it has been widely

used and modified in the simulation of the injection molding of short fiber composite material.

Flow-induced flexible fiber motion problem is more complicated than the flow-induced rigid fiber motion problem. Flexible threadlike particle motion in the shear flow was studied by Forgacs and Mason (1959). They concluded that a fiber's deformation becomes larger with the increase of the length. Different levels of deformation are caused by different lengths of the fiber. Springy rotation, snake rotation, helix rotation, and coil formation are typical flexible fiber deformation and rotation patterns as shown in Fig. 2.2.

To solve the flow-induced flexible fiber motion theoretically, Yamamoto and Matsuoka (1993) modeled the fiber as a bead-chain. They applied a similar concept of dumbbell used in the experiments. Spheres are lined up with deformable bonds. They confirmed that rotation frequency becomes higher with the fiber's deformation becomes more intensively. Slowicka *et al*. (2015) modeled the flexible fiber in a similar way. Wang *et al*. (2006) applied a rod-chain model to simulate a flexible fiber motion in the simple shear flow.

Arbitrary-Lagrangian-Eulerian (ALE) (Donea *et al*. 1999) is used widely as a computational method for solving fluid-structure interaction problem. The mesh of an ALE kinematical description of the fluid domain can displace independently of the fluid motion. The ALE improves accuracies of the calculation and alleviates excessive distortion of the computational mesh. For the flow-induced particle motion problem, however, large translation and rotation occur in the computation. The ALE is incapable to withstand very large computational mesh displacement, and re-mesh is inevitable. Transformation of data from the previous mesh to the current mesh is a tedious work in which accuracy of calculation is compromised.

Immersed Boundary (IB) method (Peskin 2002) is another computational solution in which the fluid applies a fixed space, the Eulerian description. The mesh of the fluid is no longer moved to confirm the surface of the particle. Two domains are linked by an interaction equation named 'the Dirac delta function'. Moving mesh and re-mesh are avoided in the IB method. Nonetheless, the accuracy of the IB method is not better than methods with the conformed interface between the two domains.

Both fluid and solid using the Lagrangian description is the third way to solve fluid-structure interaction problems. Smoothed Particle Hydrodynamics (SPH), Moving Particle semi-implicit (MPS) method, or Discrete element method (DEM) are methods utilizing this idea. Since both the solid and fluid are in the Lagrangian configuration, two domains can be solved together without using a specific coupling strategy.

Regardless of the configuration introduced above, there are two main coupling strategies, i.e., partitioned coupling method and monolith coupling method. The partitioned method (Park *et al*. 2001) means that the fluid domain and the solid domain are calculated separately. Then, the explicit or implicit coupling strategy is applied to couple the two domains together. The monolith coupling method (Tezduyar *et al*. 2006) means that two domains are calculated simultaneously in one equation. The monolith method is more complicated than the partitioned method, but more stable generally.

Many researches have been developed to solve flow-induced particle motion problems with computational methods discussed above. Hu *et al*. (1992) simulated rigid sphere particles motion in the fluid. Navier-stokes was the governing equation, and it was solved by the finite element method. The motion of a rigid particle is governed by Newton's second law. Fluid domain needed a remesh process after each time step. An explicit-implicit time integration coupling scheme was used to overcome instability. Sugihara-Seki (1996) neglected the inertial of fluid and applied the Stokes equation as the fluid governing equation. Zhang and Smith (2016) applied a similar

assumption and solved the Stokes equation as a quasi-static problem. Translational and angular velocity were calculated by the Newton-Raphson method. The position and the orientation were obtained by the fourth-order Runge-Kutta algorithm. Wiens and Stockie (2015) simulated the motion of a flexible fiber suspensions using immersed boundary method. The flexible fiber was modeled using a one-dimensional Kirchhoff rod theory similar to the bead-chain model. Qi (2007) also applied the bead-chain model in his calculation, but he solved the fluid with Lattice Boltzmann equation and considered the inertia of both the fluid and the solid.

3. Methodology

There are four topics in the methodology section. First, we introduce the modeling of the fluid domain. Second, the modeling and solutions of the particle are presented. The coupling strategy between the two physical domains is discussed next. Finally, we introduce the simulation scheme of the flow induced multi-particle.

3.1 Zero-Reynolds-number flow

Since the size and weight of the fiber that we are dealing with are quite small, so we assume a zero-Reynolds number-flow in this study. And the Stokes equation is used as the governing equation of the fluid domain.

The Stokes equation is a linearized equation of the Navier-Stokes equation. It is the dimensionless Navier-Stokes equation. Eq. (3.1) represents the mass conservation and Eq. (3.2) represents the momentum conservation (Malvern 1977).

$$\nabla^* \cdot \mathrm{V}^* = 0 \tag{3.1}$$

$$Re\left(\frac{\partial \mathrm{V}^*}{\partial t^*} + \mathrm{V}^* \cdot \nabla^* \mathrm{V}^*\right) = -\nabla^* \cdot (p^* \mathrm{I}) + \nabla^* \cdot [(\nabla^* \mathrm{V}^*) + (\nabla^* \mathrm{V}^*)^T] \tag{3.2}$$

Variables with superscript '*' in the Eq. (3.1) and Eq. (3.2) denotes that the variables are dimensionless variables. V, p, t and ∇ represent the velocity vector, the pressure, the time, and the gradient operator, respectively. Eqs. (3.1) and (3.2) were obtained from the dimensional Navier-Stokes equation according to the dimensionless variables (Zhang 2013).

Eq. (3.3) shows an expression of the Reynolds number Re.

$$Re = \frac{\rho_f V_c L_c}{\mu} \tag{3.3}$$

where, ρ_f, V_f, L_c and μ are the density of the fluid, the characteristic flow velocity, the characteristic length, and the viscosity, respectively. A flow with high viscosity and a low velocity leads to a low Reynolds number, such as the flow in the injection molding process. As we apply a zero Reynolds number in the calculation, the entire term on the left side of Eq. (3.2) becomes zero. Meanwhile, the inertia and the time-dependent term of the fluid vanishes. Therefore, we obtain the final fluid domain governing equation Eq. (3.4) and Eq. (3.5). Dimensionless superscript '*' is ignored in those equations for simplifications.

$$\nabla \cdot \mathrm{V} = 0 \tag{3.4}$$

$$-\nabla \cdot \{-p\mathrm{I} + [(\nabla \mathrm{V}) + (\nabla \mathrm{V})^T])\} = 0 \tag{3.5}$$

Eq. (3.4) and (3.5) are time-independent equation representing a quasi-static problem. Solving a quasi-static Stokes equation is easier and faster than solving a dynamic Navier-Stokes equation. An acceptable accuracy can be obtained in the solving low Reynolds number problem with Stokes equation compared to that applying a Navier-Stokes equation.

According to the Ladyzhenskaya-Babuska-Breezi (LBB) condition which is also known as the inf-sup condition (Reddy and Gartling 1985), the interpolation function of the pressure should be one order low than the interpolation function of the velocity based on the differential order of each term in the governing equation. Therefore, the mixed finite element is applied to solve Eq. (3.4) and Eq. (3.5) simultaneously. The Galerkin finite element method discretizes the governing equation from the strong form to the weak form. Integration of multiplication of residual of governing equation and weight function is shown in Eq. (3.6) to Eq. (3.8). They are mass conservation, momentum conservation in the x-direction, and momentum conservation in the y-direction, sequentially.

$$\int_{\Omega} \left\{\frac{\partial u}{\partial x} + \frac{\partial v}{\partial y}\right\} Q dx dy = 0 \tag{3.6}$$

$$\int_{\Omega} \left\{-\frac{\partial}{\partial x}\left[-p + 2\frac{\partial u}{\partial x}\right] - \frac{\partial}{\partial y}\left[\frac{\partial v}{\partial x} + \frac{\partial u}{\partial y}\right]\right\} w dx dy = 0 \tag{3.7}$$

$$\int_{\Omega} \left\{-\frac{\partial}{\partial x}\left[\frac{\partial v}{\partial x} + \frac{\partial u}{\partial y}\right] - \frac{\partial}{\partial y}\left[-p + 2\frac{\partial v}{\partial y}\right]\right\} w dx dy = 0 \tag{3.8}$$

In Eq. (3.6) to Eq. (3.8), u and v represent fluid velocity in the x-direction and in the y-direction. Terms Q and w are different weighting function (Reddy and Gartling, 1985). Distmesh, a free mesh tool (Oersson and Strang, 2012), was applied to discretize the geometry of the fluid domain. Finally, discretized governing equations can be written into a matrix form, as shown in Eq. (3.9).

$$K_f \cdot X\left(V_x, V_y, P\right) = F(F_x, F_y) \tag{3.9}$$

Herein, K_f is stiffness matrix generated by the mixed finite element method. $X\left(V_x, V_y, P\right)$ represents known and unknown values vector, where V_x, V_y, and P represent velocities in the x-direction, velocities in the y-direction, and pressure, respectively. Term F is forced vector of fluid domain, where F_x and F_y are forces in the x-direction and forces in the y-direction.

Fig. 3.1 shows a schematic diagram of a rectangular particle immersed in the Poiseuille flow and the boundary condition of the fluid domain. The Poiseuille flow profile is incorporated on the inlet. The do-nothing boundary condition is applied to the outlet. The non-slip boundary condition is incorporated on the top of the fluid domain, the bottom of the fluid domain, and the surface of the rectangular particle. A pressure boundary condition on the outlet is set to equal to zero to avoid singularity in the calculation.

The distributions of the velocity, distributions of the pressure, and distributions of the force in the fluid domain are obtained by solving Eq. (3.9). Only the data on the interface between the fluid domain and the rectangular particle is useful and is extracted from those results. To meet the requirements of compatibility, i.e., the velocity and the force on the interface are equivalent on both domain, results of velocities and forces on the interface of the fluid domain will be passed to the particle solver to calculate the motion of the particle.

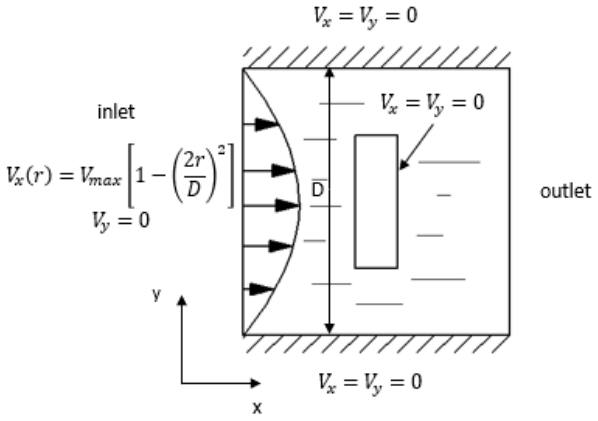

Fig. 3.1 A rectangular particle is immersed in the Poiseuille flow

3.2 Particle's dynamics

Because of the large displacement, the large rotation, and the large deformation in the particle's motion, the particle's motion is treated as a non-linear geometric dynamic problem. The particle is modeled in the two-dimensional domain. Total-Lagrangian (TL) incremental finite element method can deal with the non-linear geometry. Linear material defines the property of the particle. Bathe method, a time integration method integrates the semi-discrete equation resulted from the Total-Lagrangian method over the time domain.

Total-Lagrangian method measures and calculates everything on the initial referential configuration. Displacements are obtained step by step. Using the virtual work and the energy conservation obtains the governing equation of the particle in the current configuration, as shown in Eq. (3.10) (Reddy 2004).

$$\delta W = \int_{{}^2\Omega} {}^2\sigma : \delta({}_2e)\, d\, {}^2\Omega - \delta({}^2R) = 0 \tag{3.10}$$

Here, δW is the virtual work of the entire particle which should be equal to zero as the energy conservation. Index '2', both in superscript and subscript, indicates the configuration: current configuration. σ represents the Cauchy stress. $\delta({}_2e)$ is the virtual linear engineering strain increment. $\delta({}^2R)$ is the virtual work of the external forces. The Second Piola-Kirchhoff (2PK) stress 'S' and the Green Lagrangian strain 'E' are utilized to convert Eq. (3.10) from the current configuration to the referential configuration, as shown in Eq. (3.11).

$$\int_{{}_0\Omega} {}_0S : \delta({}_0\varepsilon)\, d\, {}^0\Omega + \int_{{}_0\Omega} {}^1S : \delta({}_0\eta)\, d\, {}^0\Omega = \delta({}^2_0R) - \delta({}^1_0R) \tag{3.11}$$

Similar to the function and the position of the index used in Eq. (3.10), index '1' represents the variable in the previous configuration of the current configuration '2'. Index '0' represents the referential configuration. $\delta({}_0\varepsilon)$ is the virtual work of the linear term of the strain. $\delta({}_0\varepsilon)$ is the virtual work of the nonlinear term of the strain. $\delta({}^2_0R)$ is the external force virtual work in the current configuration. $\delta({}^1_0R)$ is the elastic potential energy generated by the virtual work in the

previous configuration. Equation (3.11) can be simplified to a matrix form, Eq. (3.12). Here, K_T is the tangent stiffness matrix of the particle. U is the displacement of the particle. ${}^{2}_{0}F_{External}$ and ${}^{1}_{0}F_{Internal}$ correspond to the $\delta({}^{2}_{0}R)$ and $\delta({}^{1}_{0}R)$, respectively.

$$K_T U = {}^{2}_{0}F_{External} - {}^{1}_{0}F_{Internal} \tag{3.12}$$

To include the inertia and the energy dissipation of the particle, the mass matrix, and the damping matrix are calculated. Since the mass conserves through different configurations, the mass of the particle in the referential configuration is equal to the mass of the particle in the further configurations. In Eq. (3.14), we calculated the mass matrix of the particle in the referential configuration. ρ_s represents the density of the particle. In Eq. (3.14), the Rayleigh proportional damping provides an empirical way to involve the energy dissipation of the particle. Weighting coefficient α and β result from the natural mode of the system combining with a given damping ratio (Burnett 1987).

$$M = \int_{{}^{0}\Omega} \rho_s \, d \, {}^{0}\Omega \tag{3.13}$$

$$C = \alpha M + \beta K \tag{3.14}$$

Entire governing equation Eq. (3.15) is a second ordinary differential equation. To integrate over the time domain, we applied the Bathe method which is a finite-difference based method. Tangent stiffness matrix $K_t(U_{(i-1)})$ refers that the motion of the particles is a non-linear problem. The Newton-Raphson iteration method is used to solve the non-linear equation. Subscripts 'i' and 'i-1' indicate the order of the iteration.

$$M\ddot{U}_{(i)} + C\dot{U}_{(i)} + K_t(U_{(i-1)})U_{(i)} = {}^{2}_{0}F_{external} - {}^{1}_{0}F_{internal}(U_{(i-1)}) \tag{3.15}$$

Bathe method (Bathe, 2007) has two sub-steps. In the first half-time step, displacements and velocities of the particle are calculated according to the Newmark trapezoidal rule. In the second half-time step, displacements and velocities of the particle are calculated according to the three-point Euler backward method.

Only the displacements and the velocities on the nodes of the particle's surface are needed. The displacement of the particle changes the geometry of the interface. We utilized the displacements of the particle to update the mesh of the fluid domain, which meets a requirement of the geometric compatibility in the coupling. The velocities on the particle's surface in Eq. (3.9) play as the essential boundary conditions of the fluid calculation, which meets a requirement of the kinematic compatibility in the coupling.

3.3 Explicit partitioned coupling

Solutions of the fluid and the particle have been introduced in the previous sections independently. To couple those two solutions together, we derived an explicit coupling method. Three coupling compatibilities including geometric compatibility, kinematic compatibility, and dynamic compatibility, need to be satisfied by handling the displacements, the velocities, and the forces appropriately between the two domains. Fig. 3.2 shows an entire coupling scheme schematic diagram.

The fluid domain was solved first. We extracted the forces on the interface from solutions of

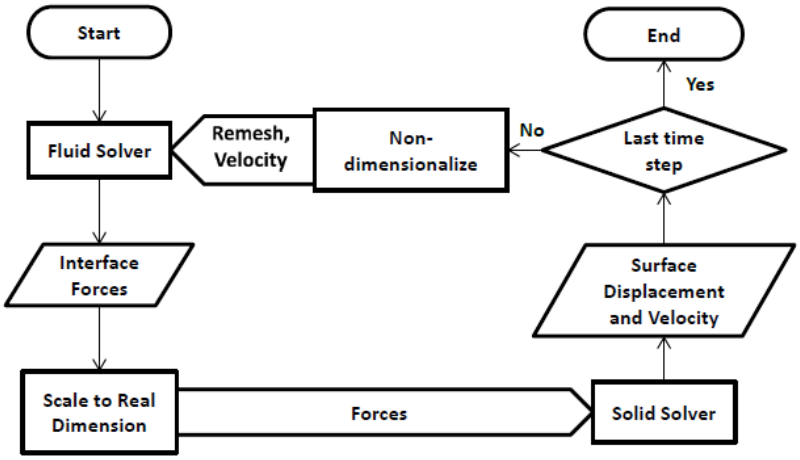

Fig. 3.2 Explicit partitioned coupling scheme flowchart

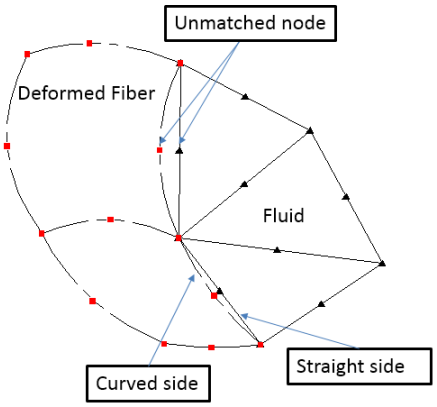

Fig. 3.3 Matching element on the interface between two domains

the fluid solver. Since the fluid domain was written in the dimensionless form and the particle dynamic equation was formulated with the physical unit without dimensionless, before delivering the forces the fluid exerting on the particle to the solid solver to solve motions of the particle, the dimensionless forces need to be scaled to the dimensional forces.

To meet the requirement of dynamic compatibility, forces sourced from the fluid domain are incorporated into Eq. (3.15) as the natural boundary condition of the solid solver. Then, the solid solver is marched forward one time-step. Velocities and displacements on the particle's surface are calculated. Before delivering the velocities and the displacements from the solid solver to the fluid solver, the velocities and the displacements are translated into dimensionless data.

To meet the requirement of geometric compatibility, a mesh tool named 'Distmesh' is applied to re-mesh the fluid domain according to the result of the new geometry of the particle's surface. We applied the quadrilateral element for the particle and a 6-node triangular element for the fluid domain. Both elements are the quadratic element. The apex of the element of each domain matches to each other, as shown in Fig. 3.3. There is a small gap between the midpoint for a pair of matched elements. Only the accuracy of the midpoint is influenced. Although a deformed particle

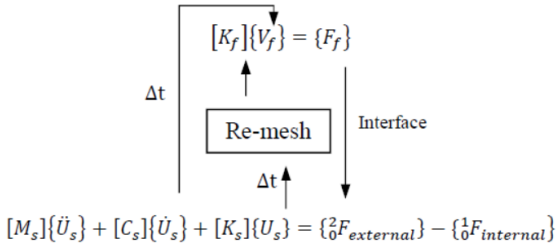

Fig. 3.4 Explicit partitioned coupling scheme between two governing equations

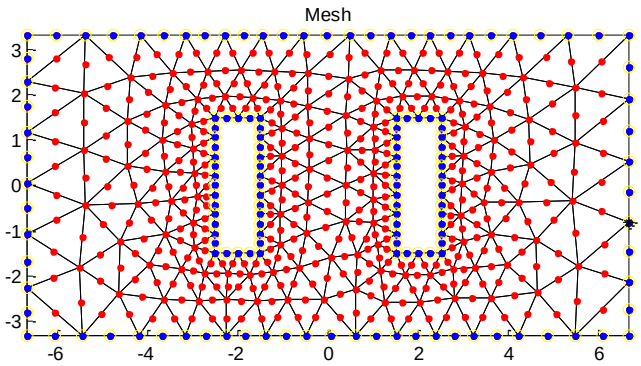

Fig. 3.5 Mesh of two rectangular particles immersed in the fluid domain

generates curved side of a quadrilateral element, the error caused by the gap is ignored. It is easy to transfer the data between to domain over the matching.

To meet the requirement of the kinematic compatibility, after re-mesh, the velocities on the surface of the particle are incorporated to the fluid domain on the matched node as the essential boundary condition. A coupling mainly takes places between two governing equations: Eq. (3.9) and Eq. (3.15). Fig. 3.4 illustrates the coupling scheme from a perspective of the governing equations.

3.4 Multi particles

The derived method can be applied to simulate flow-induced multi-particle motion. Fig. 3.5 shows that two rectangular particles are immersed in a rectangular fluid domain. We refined the mesh surrounding the particles as what we do in the simulation of a single particle.

The coupling algorithm is the same as shown in Fig. 3.2. We modified the calculation of the particle to involve more than one particle. Since the motions of two particles are independent, they are calculated simultaneously as shown in Eq. (3.16). Eq. (3.16) is equivalent to calculate Eq. (3.15) twice independently for two particles.

$$\begin{bmatrix} M^1 & 0 \\ 0 & M^2 \end{bmatrix} \begin{Bmatrix} \ddot{U}^1_{(i)} \\ \ddot{U}^2_{(i)} \end{Bmatrix} + \begin{bmatrix} C^1 & 0 \\ 0 & C^2 \end{bmatrix} \begin{Bmatrix} \dot{U}^1_{(i)} \\ \dot{U}^2_{(i)} \end{Bmatrix} + \begin{bmatrix} K^1_{t\,(i-1)} & 0 \\ 0 & K^1_{t\,(i-1)} \end{bmatrix} \begin{Bmatrix} U^1_{(i)} \\ U^2_{(i)} \end{Bmatrix} = \begin{Bmatrix} {}_0^2F^1_{external} - {}_0^1F^1_{internal}(U^1_{(i-1)}) \\ {}_0^2F^2_{external} - {}_0^1F^2_{internal}(U^2_{(i-1)}) \end{Bmatrix} \tag{3.16}$$

Table 4.1 Parameters of an elliptical particle immersed in the Couette flow

	Parameter
Type of flow	Double Couette
Viscosity $(\mathrm{N}\cdot\mathrm{s})/\mathrm{m}^2$	17
Fluid domain height: 2h	$2\mathrm{h} = 0.36$ m
V_c (m/s)	$V_c = 0.027$ mm/s
Shear rate: $\dot{\gamma}$ (1/s)	$\dot{\gamma} = 0.15\ (1/s)$
Fiber density ρ_s (kg/m^3)	$\rho_s = 1300$ kg/m^3
Long axis length	Ellipoid fiber: $\mathrm{a} = 9$ mm
Fiber ratio: re	$\mathrm{re} = 3$
Time step $\Delta\mathrm{t}$ (s)	$\Delta\mathrm{t} = 0.025$
Young's Modulus: E (Pa)	37e9
Damping ratio: ζ	$\zeta = 0$

In the simulation of multi-particle, calculation of the fluid domain is almost the same as what we did for the simulation of a single particle. More non-slips boundary conditions are added for extra particles. Forces on locations of all particle's interface need to be extracted.

The derived method is a mesh-based method, we cannot deal with the contact of two immersed particle by far. Two particles approaching each other too closely also causes low mesh quality which will lead to inaccurate calculations. Those are limitations of the derived method for simulations of the flow-induced multi-particle.

4. Results and discussion

Results of simulations with the derived computational method are shown in this section. Validation of the derived method is presented first. Then, influences of the boundary effect, the shape of a particle, the aspect ratio of a particle, and the density of a particle on the flow-induced particle motion were investigated. Simulations of flow-induced motion of two particles in the double Couette flow are presented. Finally, a simulation of immersed flexible fiber motion is presented.

4.1 Validation

To verify the derived method, we compared the result of our simulation with Jeffery's theory, Eq. (1.1). The simulation is an elliptic particle immersed in the Couette flow. Parameters used in the simulation are shown in Table 4.1.

Viscosity 17 $(\mathrm{N}\cdot\mathrm{s})/\mathrm{m}^2$ is the same as that used in the Stover and Cohen's experiment (1990). Fiber's information was provided by Kuraray (2018). Jeffery's theory assumes a particle is immersed in an unbounded fluid domain. To eliminate the boundary effect, we applied a large fluid dimension which the height is about 40 times longer than the length of the long axis of the particle. The mesh of the particle and the fluid domain are shown in Fig. 4.1. To ensure the simulation stable and meet the low Reynold's number assumption, a low characteristic velocity was used. Density ρ_s and Young's Modulus E of the particle is defined by the polymer material.

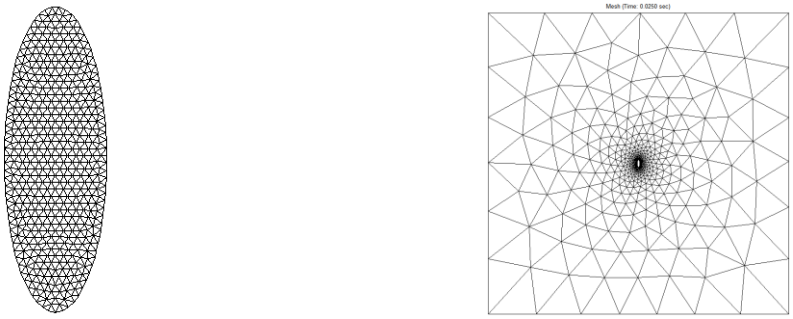

(a) (b)

Fig. 4.1 (a) Mesh of the elliptical particle; (b) Mesh of the approximately unbounded fluid domain

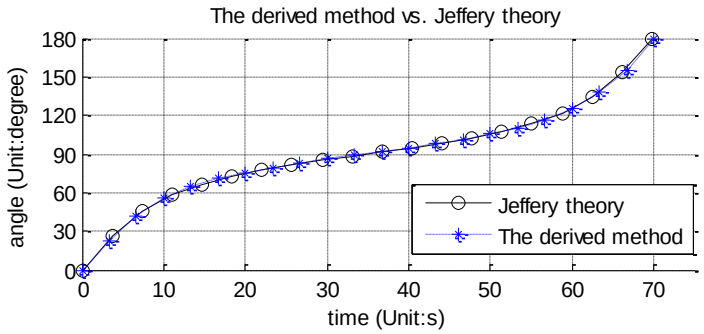

Fig. 4.2 Comparison between Jeffery's theory and the derived method on the motion of flow-induced ellipsoid particle rotation

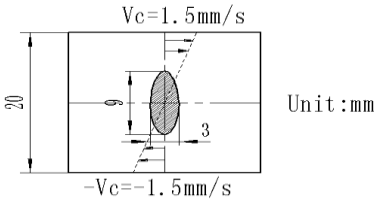

Fig. 4.3 Geometries and dimensions of an ellipsoidal fiber in a bounded double Couette flow

Results of the simulation compared with Jeffery's theory is shown in Fig. 4.2. It shows the particle's rotation angle with respect to time. The result of the derived method matches Jeffery's theory. This comparison validates the derived method, and further simulation with the derived method would be acceptable.

4.2 Boundary effect

Boundary effect takes places when the wall of the fluid domain is relatively close to the particle, which influences the motion of the particle. In this section, an ellipsoid particle is immersed in a relatively small size of the channel, and the flow is called a bounded flow. Fig. 4.3 shows an elliptical particle immersed in the double Couette flow, which is the setup of the simulation in this section. Compared to an unbounded flow as shown in Fig. 4.1(b), the only

Table 4.2 Parameters of an ellipsoidal fiber in unbounded and bounded double Couette flow

	Unbounded	Bounded
Type of flow	Double Couette	
Viscosity $(\mathrm{N}\cdot\mathrm{s})/\mathrm{m}^2$	17	
Fluid domain height: 2h	$2\mathrm{h} = 0.36$ m	$2\mathrm{h} = 0.02$m
V_c (m/s)	$V_c = 27$ mm/s	$V_c = 1.5$ mm/s
Shear rate: $\dot{\gamma}$ (1/s)	$\dot{\gamma} = 0.15\ (1/s)$	
Fiber density ρ_s ($\mathrm{kg/m}^3$)	$\rho_s = 1300\ \mathrm{kg/m}^3$	
Long axis length	Ellipoid fiber: $\mathrm{a} = 9$ mm	
Fiber ratio: re	$\mathrm{re} = 3$	
Time step Δt (s)	$\Delta\mathrm{t} = 0.025$	
Young's Modulus: E (Pa)	37e9	
Damping ratio: ζ	$\zeta = 0$	

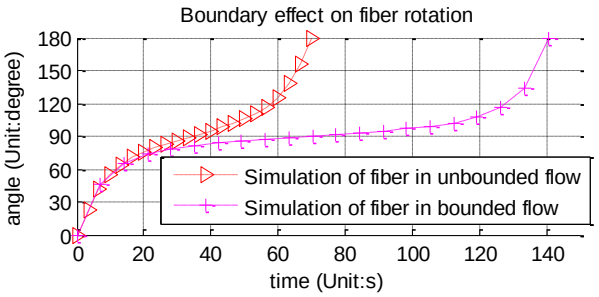

Fig. 4.4 An elliptical particle rotation in the bounded flow and the unbounded flow

Table 4.3 Parameters of an elliptic particle and a rectangular particle immersed in the double Couet te flow

	Ellipsoid fiber	Rectangular fiber
Type of flow	Double Couette	
Viscosity $(\mathrm{N}\cdot\mathrm{s})/\mathrm{m}^2$	17	
Fluid domain height: 2h	$2\mathrm{h} = 0.02$ m	
V_c (m/s)	$V_c = 1.5$ mm/s	
Shear rate: $\dot{\gamma}$ (1/s)	$\dot{\gamma} = 0.15\ (1/s)$	
Fiber density ρ_s ($\mathrm{kg/m}^3$)	$\rho_s = 1300\ \mathrm{kg/m}^3$	
Long axis length	Ellipoid fiber: $\mathrm{a} = 3$ mm	
Fiber ratio: re	$\mathrm{re} = 3$	
Time step Δt (s)	$\Delta\mathrm{t} = 0.025$	
Young's Modulus: E (Pa)	37e9	
Damping ratio: ζ	$\zeta = 0$	

difference is the size of the fluid domain. Parameters for those two simulations are shown in Table 4.2

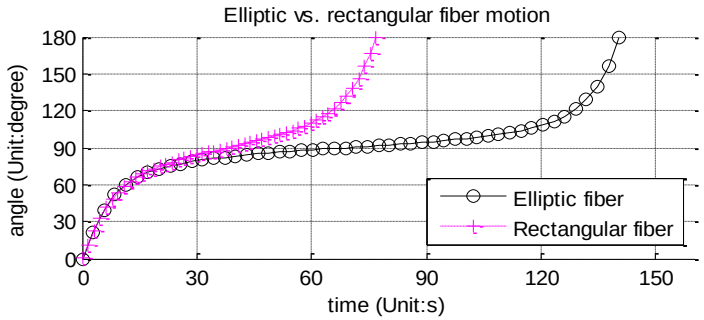

Fig. 4.5 Comparison of motions between the elliptic particle and the rectangular particle

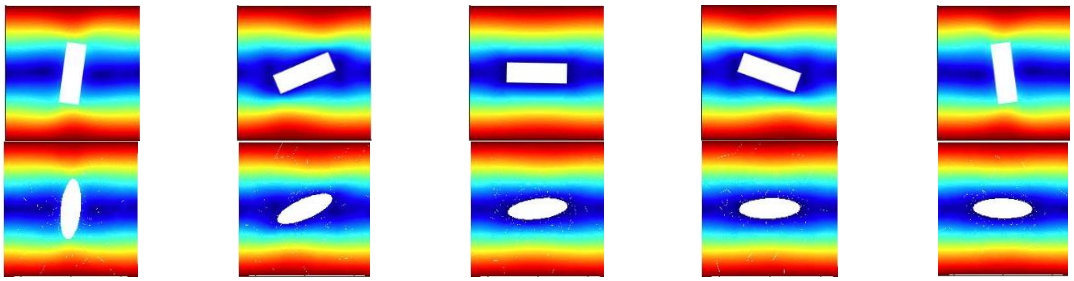

Fig. 4.6 Snapshots of the elliptic particle and the rectangular particle at sequential time instances

Table 4.4 Parameters of the flow-induced two different aspect ratio particles immersed in the Couette flow

	Large aspect ratio fiber	Small aspect ratio fiber
Viscosity $(\mathrm{N}\cdot\mathrm{s})/\mathrm{m}^2$	17	
Fluid domain height:	$2\mathrm{h} = 0.02$ m	
V_c (m/s)	$V_c = 1.5$ mm/s	
Shear rate: $\dot{\gamma}$ (1/s)	$\dot{\gamma} = 0.15\ (1/s)$	
Fiber density ρ_s	$\rho_s = 1300\ \mathrm{kg/m^3}$	
Long axis length	Ellipoid fiber: $\mathrm{a} = 3$ mm	
Fiber ratio: re	$\mathrm{re} = 9$	$\mathrm{re} = 3$
Time step $\Delta\mathrm{t}$ (s)	$\Delta\mathrm{t} = 0.025$	
Young's Modulus: E	37e9 (Pa)	
Damping ratio: ζ	$\zeta = 0$	

Fig. 4.4 shows an Angle vs. time diagram for the same elliptic particle rotation in the two different fluid domain size. The elliptic particle immersed in the bounded flow has a lower rotational frequency than that immersed in the unbounded flow. This experiment shows that the wall nearby the particle constraints the rotation of the particle and reduces the average angular velocity.

4.3 Effect of the particle's shape

To investigate the particle's shape effect on the motion, we compared motions of two different

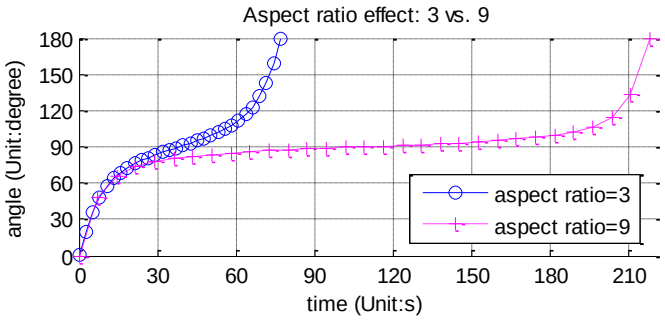

Fig. 4.7 An angel vs. time diagram of two different aspect ratio particle immersed in the Couette flow

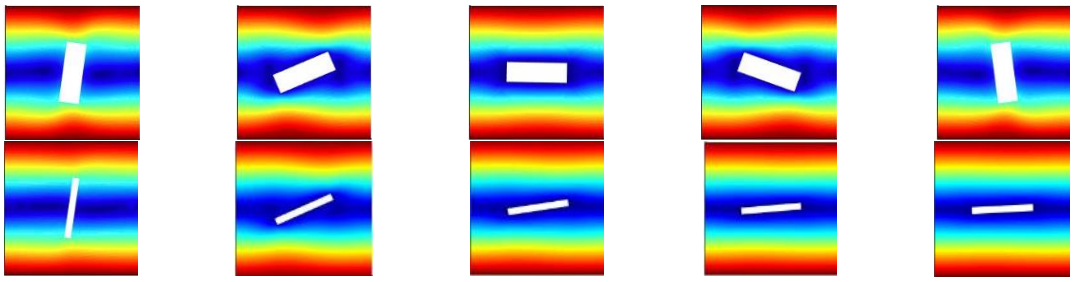

Fig. 4.8 Snapshots of the particle with an aspect ratio re=3 and the particle with an aspect ratio r e=9 at sequential time instances

Table 4.5 Parameters of experiments for the investigation of the role of the particle's density

	Case1	Case2	Case3	Case4	Case5	Case6	Case7	Case8	Case9
Type of flow	Double Couette								
Viscosity	$17\ (\mathrm{N}\cdot\mathrm{s})/\mathrm{m}^2$								
V_c (m/s)	$V_c = 1.5\ \mathrm{mm/s}$								
Shear rate: $\dot{\gamma}$ $(\frac{1}{s})$	$\dot{\gamma} = 0.15$ (1/s)								
Fiber density ρ_s ($\mathrm{kg/m^3}$)	1300	1300×10	1300×50	1300×75	1300×100	1300×175	1300×250	1300×500	1300×1000
Long axis length	Rectangular fiber: $a = 9$ mm								
Fiber ratio: re	$re = 3$								
Time step Δt (s)	$\Delta t = 0.03s$								
Young's Modulus: E (Pa)	$E = 37e9$ Pa								
Damping ratio: ζ	$\zeta = 0$								

shape particles immersed in the same fluid domain, separately. A rectangular particle and an elliptic particle were studied. Two particles have the same aspect ratio and are immersed in the same condition fluid domain, separately. Parameters of the experiments are shown in Table 4.3.

Fig. 4.5 shows an angle vs. time diagram of two flow-induced particles motions. It tells that flow-induced elliptic particle rotates slower than the flow-induced rectangular particle. Especially,

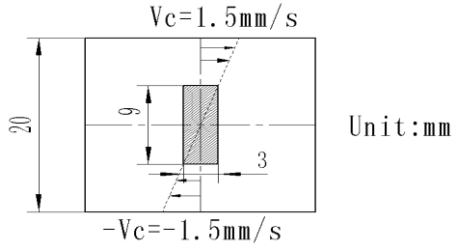

Fig. 4.9 A rectangular particle immersed in a bounded double Couette flow

at the range between about 70° to 110°, the difference of angular velocity becomes significantly. Results of simulation of two groups are presented at several time instances in sequence in Fig. 4.6. The elliptic particle takes longer time to rotate 180° compared to the rectangular particle. The elliptic particle has a streamlined shape. The flow generates less torque compared to the flow does on a rectangular particle. Therefore, the angular velocity of an elliptic particle is slower than that of a rectangular particle.

4.4 Effect of the particle's aspect ratio

Motions of two flow-induce rectangular particles with different aspect ratios are studied in this section. Two particles have the same long axis length with different aspect ratios: 9 and 3. They are immersed in the same double Couette flow, separately. Parameters for the two simulations are shown in Table 4.4.

Fig. 4.7 shows a comparison of rotations between two different aspect ratio particles. The particle with a smaller aspect ratio, re=3, has a lower rotation frequency than that of a particle with a larger aspect ratio re=9. Fig. 4.8 shows two particles' position at several time instances. The difference of the angular velocities becomes significant when the long axis of the particle approximately being parallel with the flow shear direction. A particle with a large aspect ratio generates less torque when the particle's long axis is approximately parallel with the flow shear direction.

4.5 Role of the particle's density

In many methods for the flow-induced particle motion problem, the inertia of the particle is ignored since it is light. Our derived method involves the density of the particle, which allows us to investigate the role of the particle's density on the flow-induced particle motion problem. In this study, rectangular particles with nine different densities were simulated in the bounded double Couette flow, as shown in Fig. 4.9. The parameters are shown in Table 4.5.

Particles with different densities behaved differently in the double Couette flow. Fig. 4.10 shows the angle, the angular velocity, and the angular acceleration of particles with nine different densities. Fig. 4.10 (a) shows that motions of particles with the density in the range from $1300\text{kg}/m^3$ to $1300 \times 75\text{kg}/m^3$ are similar. Their angular velocities and angular accelerations show more differences, as shown in Fig. 4.10 (b) and (c). With the decrease of the density, differences of the motion are reduced. The minimum density used in the experiment is the actual physical density of a polymer. Results show that increasing the density of a particle a little bit does not influence the result of simulations a lot on the flow-induced particle motion problems.

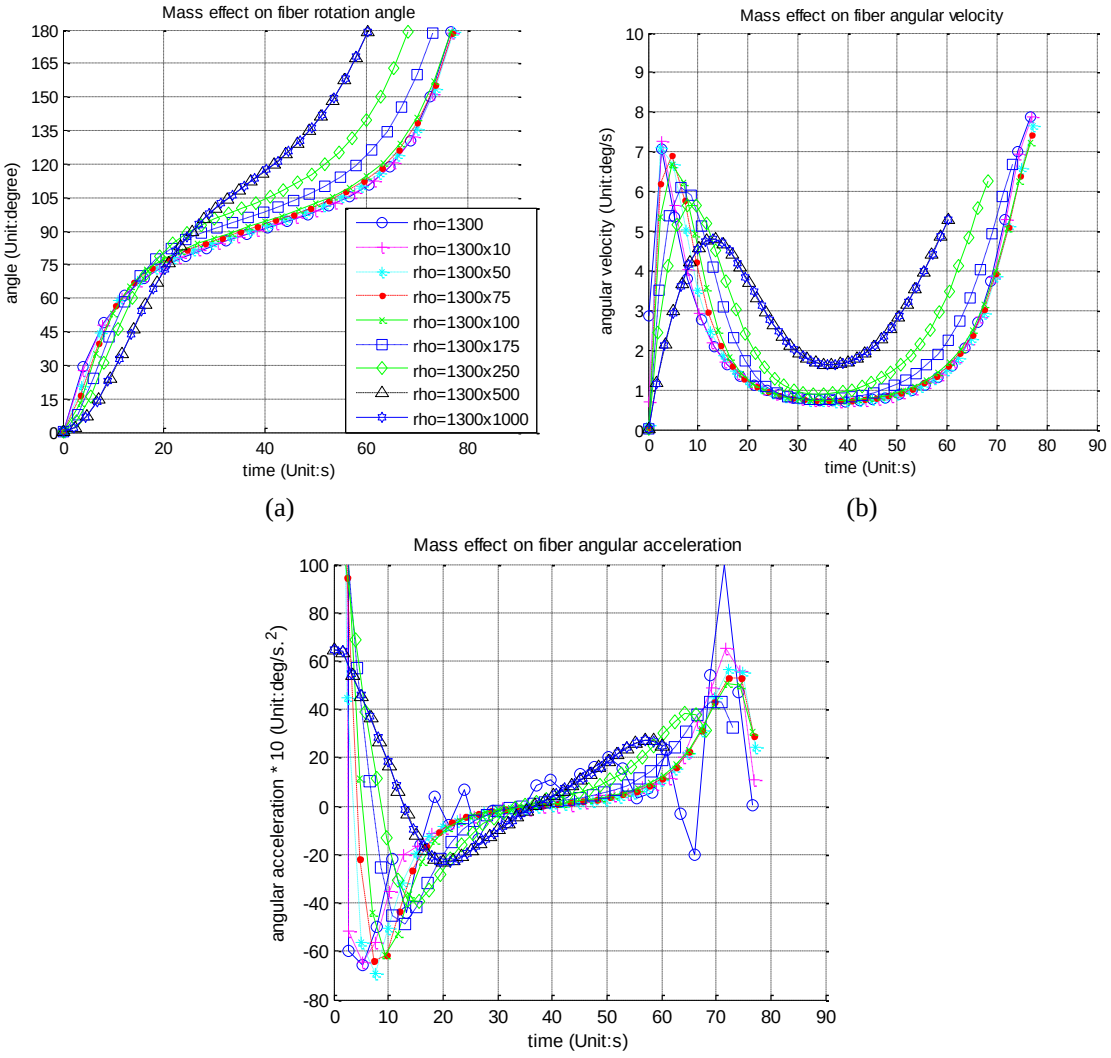

Fig. 4.10 Particles with different densities immersed in the double Couette flow. (a) Angle; (b) Angular velocity; (c) Angular acceleration

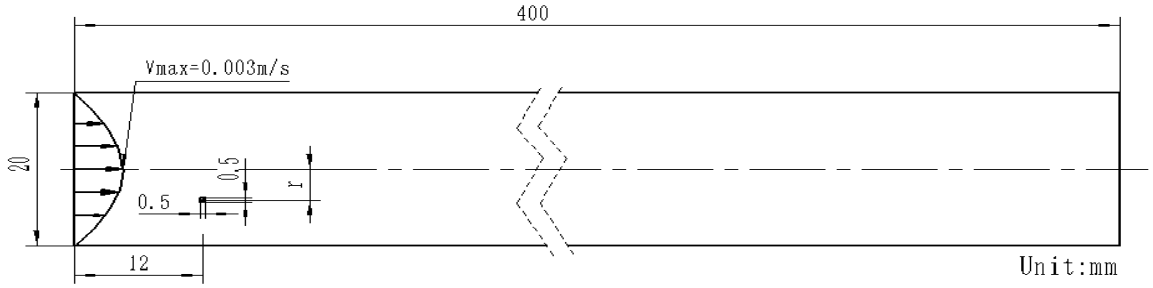

Fig. 4.11 A square particle immersed in the Couette flow

Table 4.6 Parameters of simulations that a square particle is released at the different initial position in the Poiseuille

	Case 1	Case 2	Case 3
Type of flow		Poiseuille	
Viscosity		$17\ (\mathrm{N}\cdot\mathrm{s})/\mathrm{m}^2$	
V_{max} (m/s)		$V_{max} = 0.006$	
Fiber density ρ_s		$\rho_s = 1300 \times 20\ (\mathrm{kg/m3})$	
Particle dimension		$0.5 \times 0.5\ (\mathrm{mm} \times \mathrm{mm})$	
Fiber ratio: re		$\mathrm{re} = 1$	
Eccentric: r (mm)	$\mathrm{r} = 5$	$\mathrm{r} = 6$	$\mathrm{r} = 7$
Time step Δt (s)		$\Delta t = 0.04$	
Young's Modulus:		E = 37e9 E (Pa)	
Damping ratio: ζ		$\zeta = 0$	

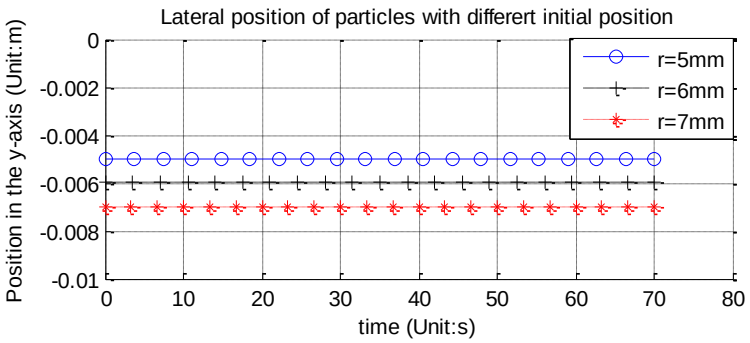

Fig. 4.12 Results of simulations that a square particle is released at different initial position in the Poiseuille flow

For extreme large densities, such as $1300 \times 500\mathrm{kg}/m^3$ to $1300 \times 1000\mathrm{kg}/m^3$, particles' motions are different from light particles. Because of their large inertia, particles' angular velocities are relatively small at the beginning. Then, their velocities become faster than any other lighter particle from about 20 sec until they rotate to $180°$, as shown in Fig. 4.10 (b). It can be explained that the motions of particles with large inertia are hard to be changed. Fig. 4.10 (a) shows that the acceleration of the particle with density $1300\mathrm{kg}/m^3$ has intense oscillation which indicates slightly instable of the simulation.

4.6 No lateral migration of the particle in the Poiseuille flow

Since the modeling of the fluid is established on the Stokes equation, the inertia of the fluid is neglected. Therefore, it is expected that no particle lateral migration should be observed in the Poiseuille flow in the simulation with the derived method. The lateral direction is the axis being perpendicular to the flow shear direction or the pipe central axis. To verify that, we simulated a square-shaped particle released from three different initial positions in the Poiseuille flow separately. A schematic diagram is illustrated in Fig. 4.11. Related parameters are shown in Table 4.6.

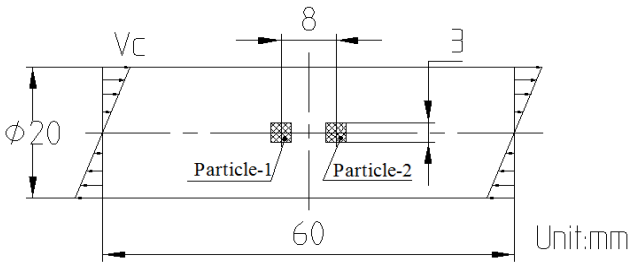

Fig. 4.13 Motions of two-particle immersed in the double Couette flow

Table 4.7 Parameters of the simulation that two square particles immersed in the double Couette flow

	Particle-1	Particle-2
Type of flow	Double Couette	
Viscosity $(\mathrm{N}\cdot\mathrm{s})/\mathrm{m}^2$	17	
Fluid domain height:	$2\mathrm{h} = 0.02$ m	
V_c (m/s)	$V_c = 1.5$ mm/s	
Shear rate: $\dot{\gamma}$ (1/s)	$\dot{\gamma} = 0.15\ (1/s)$	
Fiber density ρ_s	$\rho_s = 1300\ \mathrm{kg/m}^3$	
Long axis length	Square particle: $\mathrm{a} = 3$ mm	
Fiber ratio: re	$\mathrm{re} = 1$	
Time step $\Delta\mathrm{t}$ (s)	$\Delta\mathrm{t} = 0.025$	
Young's Modulus: E	37e9 (Pa)	
Damping ratio: ζ	$\zeta = 0$	

The lateral positions of three particles in the simulations are plotted on the same coordinate as shown in Fig. 4.12. All three particles translated straightforwardly from the initial position without any displacement in the vertical direction in the experiment. No lateral migration of any particle immersed in the Poiseuille flow is observed in the simulation. This result meets the prediction because Segré-Silberberg effect should not appear in the flow with a zero inertia.

4.7 Two-particle motion in the Couette flow

The existence of another particle may influence the motion of each other. Two particles immersed in the double Couette flow were simulated, as shown in Fig. 4.13. Table 4.7 shows parameters used in the simulation.

The simulation shows that particles influence the motion of each other. Lateral migrations are observed in the simulation, as shown in Fig. 4.14. Two particles drift away from each other in the vertical direction. Fig. 4.15 shows that two particles oppositely migrate away from an initial position in the vertical direction. Distance in the vertical direction between two particles keeps increasing until about 70 sec. Influence of particles on each other diminishes with the increasing of the distance between two particles in both the vertical and the horizontal direction. Fig. 4.16 shows two particles position in the horizontal direction. The distance keeps increasing in the horizontal direction infinitely since the two particles are in regions with the different flow velocity.

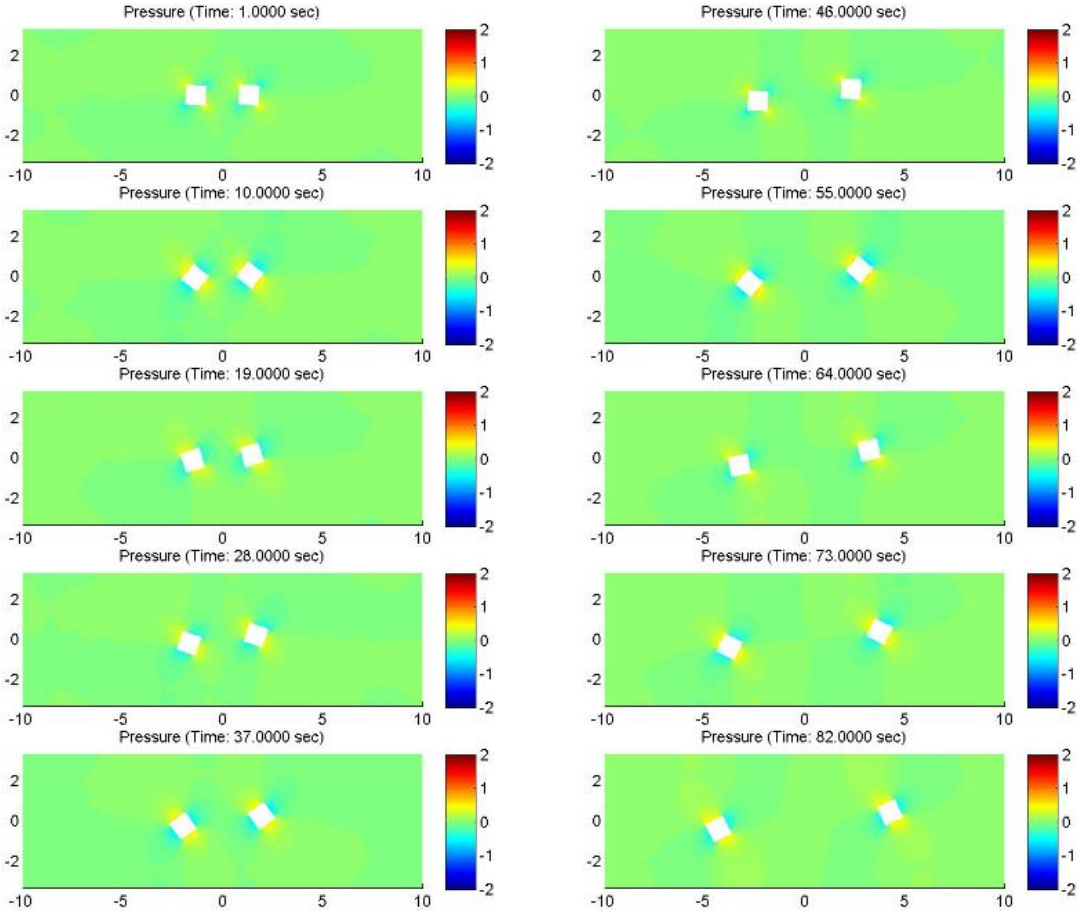

Fig. 4.14 Double Couette flow-induced two square particles motion with fluid pressure distribution

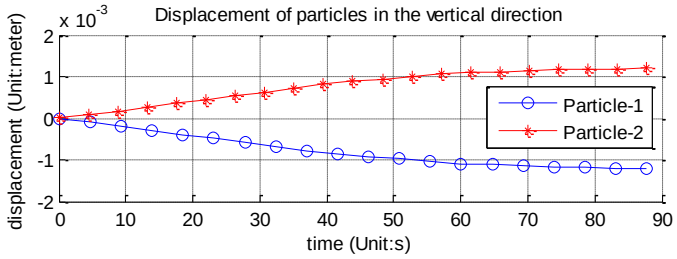

Fig. 4.15 Vertical displacement vs. time diagram of two particles immersed in the double Couette flow

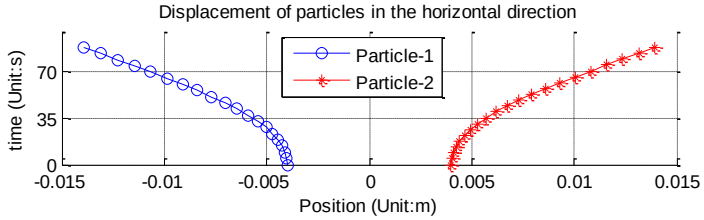

Fig. 4.16 Time vs. horizontal displacement of two particles immersed in the double Couette flow

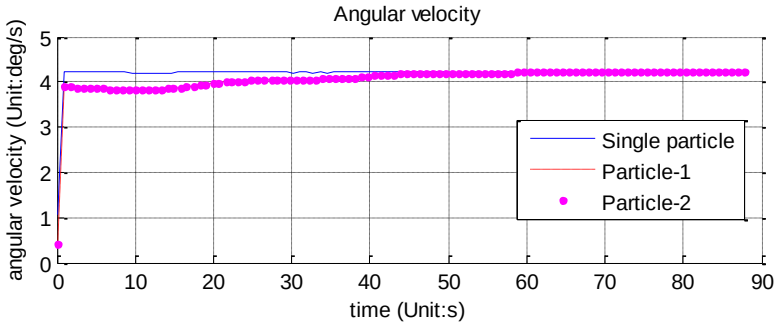

Fig. 4.17 Angular velocity vs. time diagram of a single particle and one of the two particles immersed in the double Couette flow

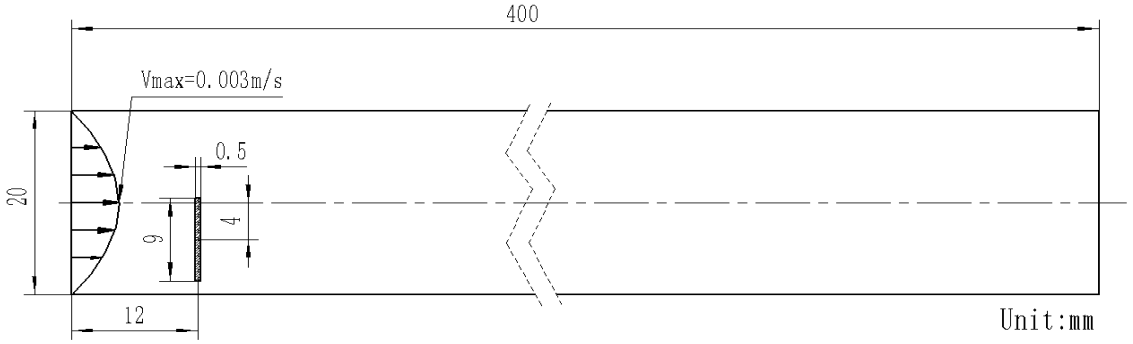

Fig. 4.18 A flexible fiber immersed in the Poiseuille flow

Table 4.8 Parameters of a simulation that flexible fiber immersed in the Poiseuille flow

Parameters	
Poiseuille	Type of flow
17	Viscosity $(\mathrm{N}\cdot\mathrm{s})/\mathrm{m}^2$
$V_{max} = 0.003\ m/s$	V_{max} (m/s)
$\rho_s = 1300 \times 20\ kg/m^3$	Fiber density ρ_s ($\mathrm{kg/m^3}$)
Rectangular fiber: a = 9 mm	Long axis length
re = 18	Fiber ratio: re
$\Delta t = 0.025$	Time step Δt (s)
$37e-1$	Young's Modulus: E (Pa)
$\zeta = 0.35$	Damping ratio: ζ

The existence of another particle also influences the rotation of the particle. Fig. 4.17 shows the angular velocities of the single particle motion and two-particle motion. It shows that at the beginning angular velocity of two-particle motion is slower than that of a single particle. After about 60 sec, the mutual influence between particles is minimized with the increasing of the distance between each other. Two particles' angular velocity becomes equal to the angular velocity of a single particle. In summary, two close-by particles reduce the angular velocity of each other.

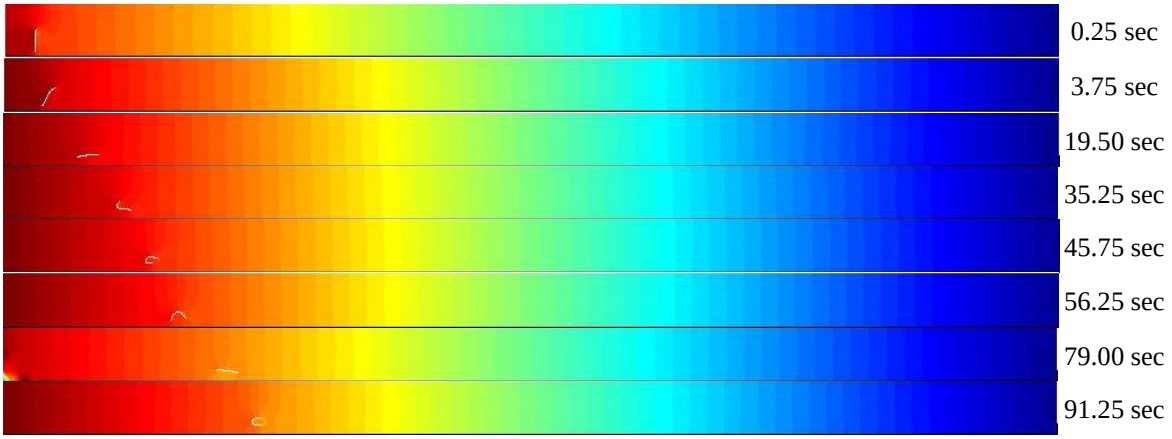

Fig. 4.19 A flexible fiber motion with pressure distribution of the Poiseuille flow at several instances in sequence

4.8 Flexible fiber motion in the Poiseuille flow

A flexible fiber immersed in the Poiseuille flow was simulated with the derived method. Geometries and dimensions of the fiber and the fluid domain are shown in Fig. 4.18. Since it is difficult to keep stable in the simulation with fiber's deformation, an extremely large damping ratio is applied in the simulation. Parameters of a flexible fiber immersed in the Poiseuille flow are shown in Table 4.8.

Deformations of the flexible fiber with pressure distributions of fluid domain are illustrated in Fig. 4.19. The flexible fiber performs snake rotation which is similar to the pattern shown in Fig. 2.2 (b). The simulation demonstrates that the derived method is able to provide the tendency of a flow-induced flexible fiber motion problem.

5. Conclusions

A computational method for solving the zero Reynolds number flow-induced particle motion problem is presented in this paper. Stokes equation is the governing equation of the fluid domain which is solved by the mixed finite element method. The particle is modeled as a non-linear geometric dynamic problem, which is solved by the Total-Lagrangian incremental finite element method and the Bathe time integration method. The explicit coupling strategy is developed to couple two domains.

Our method was validated by comparing the result of our simulation with Jeffery's theory. Influence of the boundary effect, the shape of the particle, the aspect ratio of the particle, and the density of the particle on the flow-induced particle motion were discussed. No lateral migration was observed when a particle was immersed in the Poiseuille flow in the simulation with the derived method. Two particles immersed in the double Couette flow were simulated. We observed the repulsion effect between two proximate particles. The angular velocity is also reduced with the existence of another particle nearby. The derived method is capable to simulate a flexible fiber immersed in the Poiseuille flow with an extremely large damping ratio. A snake rotation of the flexible fiber was observed in the simulation.

The derived method is able to simulate zero-Reynolds number flow-induced rigid particle motion successfully. Simulations of the flow-induced flexible fiber motion, however, is hard to keep stable which is a constraint of the derived method. The future work is to derive a stronger coupling strategy.

Acknowledgment

The research described in this paper was financially supported by the National Science Foundation Grant Number 1505530.

References

Bathe, K.J. (2007), "Conserving energy and momentum in nonlinear dynamics: A simple implicit time integration scheme", *Comput*. *Struct*., **85**(7-8), 437-445. https://doi.org/10.1016/j.compstruc.2006.09.004

Bretherton, F.P. (1962), "The motion of rigid particles in a shear flow at low Reynolds number", *J. Fl. Mech*., **14**(2), 284-304. https://doi.org/10.1017/S002211206200124X

Burnett, D.S. (1987), *Finite Element Analysis: From Concepts to Application*, Addison-Wesley Publishing Company, Whippany, New Jersey., U.S.A.

Callister, W.D.J. and Rethwisch, D.G. (2009), *Materials Science and Engineering an Introduction, Eight edition*, John Wiley & Sons, Inc, U.S.A.

Courtney, T.H. (2005), *Mechanical Behavior of Materials,* Waveland Press, Inc, Long Grove, Illinois, U.S.A.

De Corato, M., Greco, F. and Maffettone, P.L. (2015), "Locomotion of a microorganism in weakly viscoelastic liquids", *Phys*. *Rev*. *E*, **92**(5), 3008. https://doi.org/10.1103/PhysRevE.92.053008

Donea, J., Huerta, A., Ponthot, J.P. and Rodriguez-Ferran, A. (1999), "Arbitrary Lagrangian-Eulerian Methods", *Encyclopedia Comput*. *Mech*., 1-25.

Folgar, F. and Tucker, C.L. (1984), "Orientation behavior of fibers in concentrated suspensions", *J. Reinforced Plast*. *Compos*., **3**(2), 98-119. https://doi.org/10.1177/0731684484003002

Forgacs, O.L. and Mason, S.G. (1959), "Particle motions in sheared suspensions: X. Orbits of flexible threadlike particles", *J. Colloid Sci*., **14**(5), 473-491. https://doi.org/10.1016/0095-8522(59)90013-3

Ho, B.P. and Leal, L.G. (1974), "Inertial migration of rigid spheres in two-dimensional unidirectional flows", *J. Fl. Mech*., **65**(2), 365-400. https://doi.org/10.1017/S0022112074001431

Hu, H.H., Joseph, D.D. and Crochet, M.J. (1992), "Direct simulation of fluid particle motions", *Theor*. *Comput*. *Fl. Dyn*., **3**(5), 285-306. https://doi.org/10.1007/BF00717645

Jeffery, G.B. (1922), "The motion of ellipsoidal particles immersed in a viscous fluid", *Proceedings of the Royal Society of London, Series A*, **102**(715), 161-179. https://doi.org/10.1098/rspa.1922.0078

Kuraray (2018), Fibers and Textiles/Man-Made Leather/Nonwoven Fabrics/Hook-and-Loop Fasteners/Vinyl Acetate Derivatives/KURALON, Kuraray Co., Ltd, Tokyo, Japan. www.kuraray.com/products/vinylon

Malvern, L.E. (1977), *Introduction to the Mechanics of a Continuous Medium*, Prentice Hall, Inc, New Jersey, U.S.A.

Oersson, P.O. and Strang, G. (2012), Distmesh - A Simple Mesh Generator in MATLAB, Department of Mathematics, UC Berkeley, California, U.S.A. http://persson.berkeley.edu/distmesh/.

Papathanasiou, T.D. and Guell, D.C. (1997), *Flow-Induced Alignment in Composite Materials*, Elsevier, Cambridge, U.K.

Park, K.C., Felippa, C.A. and Farhat, C. (2001), "Partitioned analysis of coupled systems", *Comput*. *Meth*. *Transient Anal*., **190**(24-25), 3247-3270.

Peskin, C.S. (2002), "The immersed boundary method", *Acta Numerica*, **11**, 479-517. https://doi.org/10.1017/S0962492902000077

Qi, D. (2007), "A new method for direct simulations of flexible filament suspensions in non-zero raynolds number flow", *Int. J. Numer. Method Fl.*, **54**(1), 103-118. https://doi.org/10.1002/fld.1398

Reddy, J.N. (2004), *An Introduction To Nonlinear Finite Element Analysis*, *Oxford University Press*, Oxford University Press, Oxford, U.K.

Reddy, J.N. and Gartling, D.K. (1985), *The Finite Element Method in Heat Transfer and Fluid Dynamics*, CRC Press, New York, U.S.A.

Ross, R.F. and Klingenberg, D.J. (1997), "Dynamic simulation of flexible fibers composed of linked rigid bodies", *J. Chem. Phys.*, **106**(7), 2949-2960. https://doi.org/10.1063/1.473067

Segré, G. and Silberberg, A. (1961), "Radial particle displacements in poiseuille flow of suspensions", *Nature*, **189**(4760), 209-210. https://doi.org/10.1038/189209a0

Slowicka, A.M., Wajnryb, E. and Ekiel-Jezewska, M.L. (2015), "Dynamics of flexible fibers in shear flow", *J. Chem. Phys.*, **143**(12), 124904. https://doi.org/10.1063/1.4931598

Stover, C.A. and Cohen, C. (1990), "The motion of rodlike particles in the pressure-driven flow between two flat plates", *Rheologica Acta*, **29**(3), 192-203. https://doi.org/10.1007/BF01331355

Sugihara-Seki, M. (1996), "The motion of an ellipsoid in tube flow at low Reynolds numbers", *J. Fl. Mech.*, **324**, 287-308. https://doi.org/10.1017/S0022112096007926

Tan, J., Keller, W., Sohrabi, S., Yang, J. and Liu, Y. (2016), "Characterization of nanoparticle dispersion in red blood cell suspension by the lattice boltzmann-immersed boundary method", *Nanomaterials*, **6**(2), 30. https://doi.org/10.3390/nano6020030

Tezduyar, T., Sathe, S. and Senga, M. (2006), "Finite element modeling of fluid-structure interactions with space-time and advanced mesh update techniques", *Fl. Struct. Interact. Lecture Notes Comput. Sci. Eng.*, **53**, 50-81.

Wang, G., Yu, W. and Zhou, C. (2006), "Optimization of the rod chain model to simulate the motions of a long flexible fiber in simple shear flows", *Eur. J. Mech. B Fluids*, **25**(3), 337-347. https://doi.org/10.1016/j.euromechflu.2005.09.004

Wiens, J.K. and Stockie, J.M. (2015), "Simulating flexible fiber suspensions using a scalable immersed boundary algorithm", *Comput. Meth. Appl. Mech. Eng.*, **290**, 1-18. https://doi.org/10.1016/j.cma.2015.02.026

Yamamoto, S. and Matsuoka, T. (1993), "A method for dynamic simulation of rigid and flexible fibers in a flow field", *J. Chem. Phys.*, **98**(1), 644-650. https://doi.org/10.1063/1.464607

Zhang, D. (2013), *Flow-Induced Micro- and Nano-Fiber Suspensions in Short-Fiber Reinforced Composite Materials Processing*, University of Missouri, U.S.A.

Zhang, D. and Smith, D.E. (2016), "Dynamic simulation of discrete fiber motion in fiber-reinforced composite materials processing", *J. Compos. Mater.*, **50**(10), 1301-1319. https://doi.org/10.1177/0021998315590266